RSC Advances

PAPER

View Article Online
View Journal | View Issue

Cite this: *RSC Adv.*, 2026, **16**, 18257

Numerical investigation of vanadium distill-condensation *via* computational fluid dynamics

Zeli Yang,[abcd] Yong Fan,*[abcd] Yimin Zhang,[abcd] Qiushi Zheng,[abcd] Peng Liu[abcd] and Jiang Huang[abcd]

A coupled VOF-Species Transport-Discrete Phase numerical framework incorporating user-defined condensation source terms (UDFs) is developed to investigate the multiphase condensation behavior and impurity migration of $VOCl_3$ mixed vapors under nitrogen-protected conditions. The spatial evolution of vapor–liquid interfaces, heat and mass transfer, and particle transport is systematically analyzed. The results show that condensation is initiated at localized interfacial regions near the cooled wall and gradually evolves into continuous liquid film growth along the flow direction, leading to a transition from interfacial-controlled to diffusion-controlled condensation. The accumulation of non-condensable nitrogen thickens the diffusion boundary layer and suppresses condensation, while enhanced wall subcooling strengthens the thermal driving force. Their competition governs the spatial non-uniformity of condensation intensity. The synchronized attenuation of Nusselt and Sherwood numbers confirms the coupled heat and mass transfer mechanism. Most solid particles are transported along gas streamlines, yielding outlet recovery rates above 99%, whereas slight particle enrichment near the liquid film suggests a weak interception effect. These findings provide guidance for optimizing industrial distillation – condensation systems.

Received 14th February 2026
Accepted 27th March 2026

DOI: 10.1039/d6ra01311b

rsc.li/rsc-advances

1. Introduction

Vanadium oxytrichloride ($VOCl_3$) is a crucial intermediate in the vanadium chemical industry and has been extensively applied in catalysts, supercapacitors, vanadium redox flow batteries (VRFBs), and advanced vanadium alloys.[1–6] With the rapid development of renewable energy and large-scale energy storage technologies, the market demand for VRFBs continues to grow, leading to an urgent requirement for high-purity $VOCl_3$ production.[7] Industrial $VOCl_3$ is typically produced through a chlorination–distillation route, in which vanadium-bearing solids react with molten chlorides to generate gaseous $VOCl_3$. During this process, undiluted $VOCl_3$ vapor, nitrogen used as a protective atmosphere, and entrained fine solid chlorides such as NaCl and $AlCl_3$ form a complex multiphase $VOCl_3$-N_2-solid flow. The condensation and rectification behaviors of this heterogeneous mixture critically determine product purity, yield, and operational stability, thereby directly affecting process efficiency and equipment reliability.[8–11]

The $VOCl_3$-N_2-solid system exhibits pronounced non-azeotropic characteristics and strong coupling among flow dynamics, heat transfer, and mass transfer. Nitrogen serves not only as an inert protective gas but also as a typical non-condensable gas (NCG) that accumulates near the vapor–liquid interface, forming a diffusion boundary layer. This enrichment substantially increases interfacial mass-transfer resistance and weakens local condensation intensity. Meanwhile, $VOCl_3$ vapor undergoes a continuous morphological evolution from initially dispersed condensation patterns to the formation of a continuous liquid film along the cooled wall, driven by the combined effects of wall subcooling, interfacial transport resistance, and hydrodynamic shear. This evolution leads to highly localized and spatially non-uniform condensation behavior, reflecting the intrinsic intermittency of coupled heat and mass transfer under NCG-dominated conditions.

Moreover, entrained solid particles can locally disturb the flow field and interfacial structure, thereby modifying the spatial distribution of velocity, temperature, and species concentration. Such hydrodynamic interactions further influence the development of the condensate layer and the local condensation characteristics. In this study, particle motion is primarily governed by aerodynamic drag and gravitational effects, which are effectively captured within the discrete phase model (DPM) framework.

[a]*School of Resource and Environmental Engineering, Wuhan University of Science and Technology, Wuhan 430081, Hubei Province, China. E-mail: fanyong@wust.edu.cn*
[b]*State Environmental Protection Key Laboratory of Mineral Metallurgical Resources Utilization and Pollution Control, Wuhan University of Science and Technology, Wuhan 430081, Hubei Province, China*
[c]*Collaborative Innovation Center of Strategic Vanadium Resources Utilization, Wuhan University of Science and Technology, Wuhan 430081, Hubei Province, China*
[d]*Hubei Provincial Engineering Technology Research Center of High Efficient Cleaning Utilization for Shale Vanadium Resource, Wuhan University of Science and Technology, Wuhan 430081, Hubei Province, China*

Impurity migration during condensation represents another critical challenge. Fine chloride particles, including NaCl, $AlCl_3$, and $FeCl_3$, may be partially intercepted, transported, or redistributed by the liquid $VOCl_3$ condensate, which not only affects final product purity but also contributes to fouling, corrosion, and operational instability. However, the coupled mechanisms between interfacial condensation dynamics and impurity transport remain insufficiently understood, particularly for reactive metal chloride systems such as $VOCl_3$. A systematic investigation of this coupling behavior is therefore essential for improving product recovery, suppressing impurity carryover, and guiding rational design of industrial purification processes.

Substantial theoretical and numerical efforts have been devoted to vapor condensation in the presence of non-condensable gases. Based on Nusselt's classical film condensation theory,[12] modified analytical and empirical models have been developed for vapor – NCG systems. Minkowycz and Sparrow[13] proposed a boundary-layer formulation for condensation on vertical walls, emphasizing the dominant role of diffusion resistance. Colburn and Hougen[14–16] further established diffusion-layer theories, demonstrating that NCG accumulation near cold surfaces is the primary cause of heat-transfer deterioration. Denny *et al.*[17,18] applied finite-difference methods and semi-empirical correlations, revealing that low vapor velocities and elevated NCG contents markedly degrade condensation performance. Oh *et al.*[19] validated the heat-mass transfer analogy approach and confirmed its consistency with experimental measurements. These studies consistently indicate that NCG accumulation is the key factor responsible for heat-transfer suppression in multicomponent condensation processes.[20,21]

With the rapid development of computational fluid dynamics, numerical simulation has become a powerful tool for exploring multicomponent condensation mechanisms.[22,23] Jin *et al.*[24] investigated condensation of undiluted refrigerants in horizontal tubes and found that vapor-phase diffusion dominates the upstream region, whereas liquid-film resistance governs downstream heat transfer. Similar conclusions were reported by Klahm *et al.*[7] for R134a/R123 mixtures. Zhang *et al.*[25] further demonstrated that low-volatility components enhance condensation, while high-boiling constituents aggravate heat and mass transfer deterioration. Due to experimental difficulties, corrosive environments, and safety constraints, numerical modeling remains the most practical approach for investigating hazardous and non-azeotropic systems, including $VOCl_3$-based mixtures.[26–33]

Despite these advances, the condensation behavior of $VOCl_3$ vapor under nitrogen protection, together with the coupled migration of entrained solid impurities, has not yet been systematically clarified. In particular, the localized and discontinuous nature of $VOCl_3$ condensation and its interaction with particle transport remain poorly understood. Therefore, in the present work, a coupled two-dimensional VOF-Species Transport-Discrete Phase numerical framework is established, in which condensation mass and energy source terms are dynamically implemented *via* user-defined functions (UDFs). This model captures the transient evolution of vapor–liquid interfaces and particle motion within undiluted $VOCl_3$ systems under nitrogen protection, while acknowledging the inherent limitations of the two-dimensional approximation. The simulations systematically examine (1) the flow and thermal characteristics during condensation, (2) the effects of wall subcooling and NCG concentration on condensation efficiency, and (3) the migration and deposition behaviors of solid impurities. The results reveal the transition from dropwise to film-wise condensation, the resulting localized and discontinuous interfacial dynamics, and the governing role of flow structures in particle transport. These findings provide mechanistic insights and practical guidance for optimizing industrial chlorination–distillation processes and improving $VOCl_3$ purification efficiency.

2. Experimental observation and impurity analysis

2.1 Experimental setup

As schematically illustrated in Fig. 1, sodium chloride (NaCl) and aluminum chloride ($AlCl_3$) were first mixed in a sealed glass reactor and heated to form a homogeneous ionic melt. Subsequently, solid vanadium-containing precursors were introduced

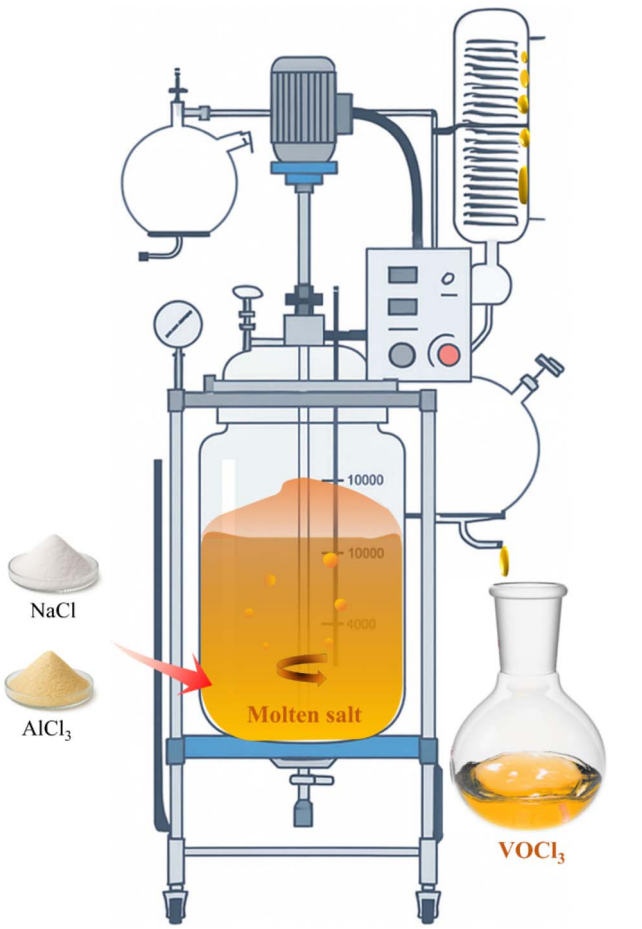

Fig. 1 Schematic diagram of experimental setup for $VOCl_3$ chlorination–condensation system.

Table 1 ICP results of impurity composition before and after distill-condensation

	Impurity content (%)									
Optimal condition (170 °C)	Na	Al	Fe	Mg	K	Cr	P	Ni	Mo	$VOCl_3$ purity (%)
Vanadium shake leachate	2.964	8.445	14.657	51.035	3.451	0.934	2.395	5.603	0.081	—
Precipitate product	13.491	6.642	2.740	8.356	1.480	0.121	0.293	0.359	0.071	—
Vanadium-rich solution	0.010	0.045	0.006	0.005	0.005	0.005	0.002	0.001	0.001	99.920
Distillate II	0.016	0.008	0.005	0.007	0.003	0.001	0.001	0.001	—	99.958
Distillate III	0.009	0.012	0.003	0.004	0.005	—	—	0.001	—	99.966
Distillate IV	0.003	0.004	0.001	0.001	0.001	—	—	—	—	99.990

to initiate the chlorination reaction, generating vanadium oxytrichloride ($VOCl_3$) vapor. The produced vapor was continuously transported by nitrogen gas and directed into a vertical glass condensation column, where phase change occurred along the cooled inner wall, and the condensed liquid $VOCl_3$ was finally collected in a downstream receiver.

During the reaction process, the initially transparent molten salt gradually turned light yellow, indicating the onset of chlorination. As the reaction progressed, dense orange $VOCl_3$ vapor was observed escaping from the upper outlet of the reactor. Upon entering the cooled condensation section, the vapor underwent rapid phase transition on the inner wall, forming dispersed condensate structures that gradually evolved into continuous flowing liquid films. This macroscopic morphological evolution reflects the typical transition from localized condensation to film-dominated condensation along the cooling surface. After condensation, a transparent light-yellow liquid product was collected and identified as $VOCl_3$.

The reactor temperature during chlorination was maintained at approximately 170 °C. Nitrogen was supplied as a carrier gas at a controlled flow rate to transport $VOCl_3$ vapor into the condenser. The condenser wall temperature was regulated through an external cooling system to provide a stable subcooling condition.

These experimental observations provide direct visual evidence of the spatially non-uniform condensation behavior and condensate film development during $VOCl_3$ condensation, which serve as important qualitative benchmarks for validating the numerical predictions of flow – thermal coupling and interfacial phase-change dynamics.

2.2 Impurity analysis *via* ICP

To evaluate reaction completeness and impurity transport behavior, both the solid raw materials and the condensed $VOCl_3$ liquid products were analyzed using inductively coupled plasma (ICP) spectrometry. Elemental concentrations of vanadium (V), aluminum (Al), sodium (Na), and trace impurities (*e.g.*, Fe, K, and Mg) were measured.

The ICP results, summarized in Table 1, indicate that vanadium is the dominant component in the condensed liquid, while only trace amounts of Al and Na originating from the ionic melt are detected. This observation suggests that the chlorination reaction effectively volatilizes $VOCl_3$, whereas the majority of non-volatile impurities remain in the molten phase. Although absolute quantitative accuracy is affected by sampling limitations and measurement uncertainties, the measured elemental trends provide meaningful qualitative validation of impurity reduction and transport behavior during condensation.

Importantly, these experimental findings support the physical assumptions adopted in the numerical model, particularly regarding impurity migration pathways and phase partitioning during condensation, and thus serve as a qualitative reference for assessing the reliability of the simulation results.

3. Numerical models and computational methods

3.1 Physical model and boundary conditions

The distillation condenser constitutes a key unit in the chlorination–distillation process for $VOCl_3$ purification. To achieve a balance between computational efficiency and physical representativeness, a two-dimensional (2D) computational domain with a size of 0.02 m × 0.2 m was established, as illustrated in Fig. 2. The domain corresponds to a representative longitudinal cross-section of the vertical condenser, where the dominant transport processes primarily develop along the streamwise and wall-normal directions. Under the present operating conditions, transverse variations along the condenser width are relatively weak, and the primary gradients of velocity, temperature, and species concentration are mainly confined within this plane. Therefore, the 2D approximation is considered adequate for capturing the essential features of flow development, interfacial phase change, and coupled heat–mass transfer behavior, while significantly reducing computational cost.

The $VOCl_3$-N_2-solid mixture enters the domain at a uniform velocity of 0.2 m s^{-1} and undergoes cooling and condensation along the isothermal wall. The inlet was specified as a velocity inlet, while the outlet was treated as a pressure outlet. The wall opposite the condenser plate was defined as a symmetry boundary, and the cooled wall was imposed as a no-slip, constant-temperature boundary. Gravity acts in the vertical direction, consistent with the actual configuration of the experimental condenser.

It should be noted that the present 2D framework is mainly intended to resolve the transient evolution of the vapor–liquid interface, the development of condensate structures, and the

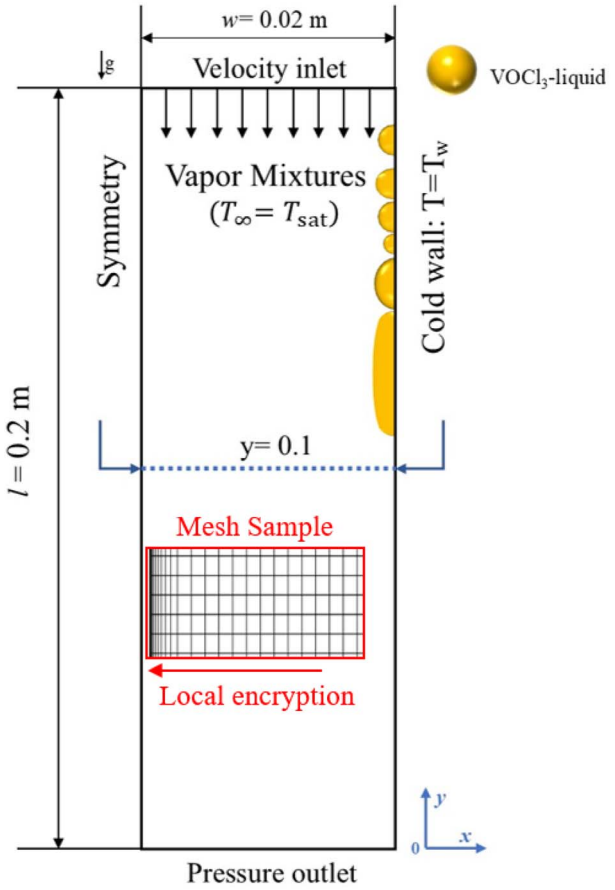

Fig. 2 Computational domain and boundary conditions.

associated heat and mass transfer processes in a representative cross-section. While certain three-dimensional effects related to spanwise flow variations are not explicitly captured, their influence is expected to be secondary under the present operating conditions. Consequently, the model is capable of providing reliable qualitative and semi-quantitative insights into the dominant condensation mechanisms and impurity transport behaviors relevant to practical $VOCl_3$ purification processes.

3.2 Governing equations and computational framework

The multiphase flow and phase-change process were simulated using the Volume of Fluid (VOF) method,[34] coupled with Species Transport and the Discrete Phase Model (DPM). The gas and liquid phases share a single set of momentum, continuity, and energy equations, with phase distribution tracked by the volume fraction α, The sum of the gas and liquid phase volume fractions is equal to 1 in each cell:

$$\frac{\partial \alpha_q}{\partial t} + \nabla \cdot (\alpha_q\, u) = 0 \tag{1}$$

$$\alpha_v + \alpha_l = 1 \tag{2}$$

The governing equations for mass, momentum, and energy are expressed as:

$$\frac{\partial \rho}{\partial t} + \nabla \cdot (\rho u) = S_m \tag{3}$$

$$\frac{\partial (\rho v)}{\partial t} + \nabla \cdot (\rho u u) = -\nabla \cdot P + \rho g + S_{pu} \tag{4}$$

$$\frac{\partial (\rho h)}{\partial t} + \nabla \cdot (\rho u h) = \nabla \cdot \left(k_{eff} \nabla T\right) + S_h \tag{5}$$

where S_m and S_h represent the mass and latent heat source terms induced by condensation.

The transport of condensable vapor species is governed by:

$$\frac{\partial (\rho Y_i)}{\partial t} + \nabla \cdot (\rho u Y_i) = -\nabla \cdot J_i + S_m \tag{6}$$

where the diffusive flux J_i follows Fick's law:

$$J_i = \rho D_{ij} \frac{\partial \omega_i}{\partial y} \tag{7}$$

The binary diffusion coefficient D_{ij} of $VOCl_3$ vapor in nitrogen is calculated using the Chapman–Enskog equation[35] based on kinetic theory.

3.3 Condensation phase-change model

Condensation is triggered when the local gas-phase temperature drops below the saturation temperature T_{sat}. In the

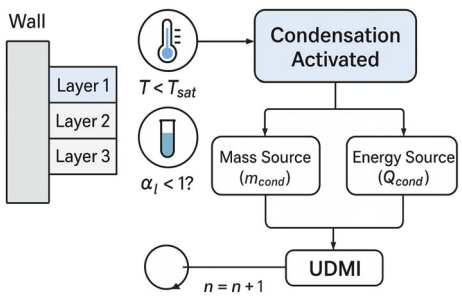

Fig. 3 Procedure of user defined function.

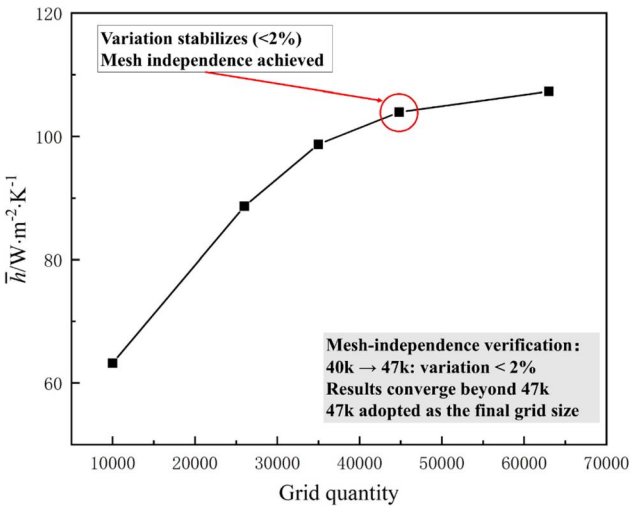

Fig. 4 Heat transfer coefficient with different grid quantities.

presence of non-condensable gas (NCG), the condensation rate is primarily governed by vapor diffusion through the gas-phase boundary layer adjacent to the interface. Accordingly, the local condensation mass flux can be expressed based on the classical diffusion-layer formulation for condensation in the presence of non-condensable gases:[13]

$$m'_{\mathrm{cond}} = C_{\mathrm{factor}} \rho D_{ij} \left. \frac{\partial Y_{\mathrm{v}}}{\partial n} \right|_{\mathrm{int}} \tag{8}$$

where ρ is the gas density, D_{ij} is the binary diffusion coefficient, Y_{v} is the vapor mass fraction, $\frac{\partial Y_{\mathrm{v}}}{\partial n}$ denotes the gradient normal to the interface, and C_{factor} is a dimensionless correction factor introduced to account for possible deviations arising from numerical discretization and local interfacial transport simplifications in diffusion-controlled condensation models.

In the present study, C_{factor} was set to 1.0, which corresponds to the assumption that the condensation rate is directly governed by the local diffusion flux without additional empirical correction. Similar treatments have been widely adopted in diffusion-layer-based condensation models when no empirical calibration data are available.[36,37] Therefore, setting $C_{\mathrm{factor}} = 1.0$ represents a physically consistent approximation for systems dominated by vapor diffusion resistance.

To further evaluate the robustness of this assumption, a brief sensitivity analysis was performed by varying C_{factor} within the range of 0.8–1.2. The predicted surface-averaged condensation heat–transfer coefficient changed by less than 4%, while the overall spatial trends of condensation intensity and vapor concentration distribution remained essentially unchanged. This result indicates that the model predictions are not highly sensitive to moderate variations in this parameter and that the adopted value provides a stable and physically reasonable representation of the condensation process.

The corresponding volumetric source terms for mass and energy in each computational cell are expressed as:

$$S_{\mathrm{m}} = m'_{\mathrm{cond}} \frac{A_{\mathrm{eff}}}{V_{\mathrm{cell}}} \tag{9}$$

$$S_{\mathrm{h}} = S_{\mathrm{m}} \cdot L \tag{10}$$

where A_{eff} is the effective interfacial area, V_{cell} is the cell volume, and L is the latent heat of condensation.

To dynamically evaluate the condensation source terms, a User-Defined Function (UDF) was developed. The algorithm sequentially scans the near-wall computational cells to identify regions satisfying condensation criteria ($T < T_{\mathrm{sat}}$ and vapor-phase dominance). For eligible cells, the local vapor concentration gradient is computed, and the corresponding mass and energy source terms are assigned. This procedure enables accurate tracking of the transient evolution of the vapor–liquid interface, the development of condensate structures, and the formation of continuous liquid films, thereby capturing the essential features of interfacial phase-change dynamics and heat–mass transfer coupling. The overall computational logic is illustrated in Fig. 3.

Thermophysical properties of the gas–liquid phases were obtained from the REFPROP 9.1 database[38] and evaluated using volume-fraction-weighted averaging:

$$\rho = \alpha_{\mathrm{v}} \rho_{\mathrm{v}} + \alpha_{\mathrm{l}} \rho_{\mathrm{l}} \tag{11}$$

$$\mu = \alpha_{\mathrm{v}} \mu_{\mathrm{v}} + \alpha_{\mathrm{l}} \mu_{\mathrm{l}} \tag{12}$$

$$\lambda = \alpha_{\mathrm{v}} \lambda_{\mathrm{v}} + \alpha_{\mathrm{l}} \lambda_{\mathrm{l}} \tag{13}$$

$$C_{\mathrm{p}} = \frac{1}{\rho} \left(\alpha_{\mathrm{v}} \rho_{\mathrm{v}} C_{\mathrm{pv}} + \alpha_{\mathrm{l}} \rho_{\mathrm{l}} C_{\mathrm{pl}} \right) \tag{14}$$

3.4 Discrete phase model (DPM) and solid–gas–liquid interaction model

The motion of entrained solid particles was simulated using the Discrete Phase Model (DPM),[39] with particle trajectories governed by:

$$\frac{\mathrm{d}\mu_{\mathrm{p}}}{\mathrm{d}t} = \frac{1}{\tau_{\mathrm{p}}} \left(\mu - \mu_{\mathrm{p}} \right) + g \left(1 - \frac{\rho}{\rho_{\mathrm{p}}} \right) \tag{15}$$

where $\tau_{\mathrm{p}} = \frac{\rho_{\mathrm{p}} {d_{\mathrm{p}}}^2}{18\mu}$ is the particle relaxation time.

Particles were injected at the inlet with an initial velocity identical to the gas flow and were tracked under the assumption of negligible interphase heat and mass transfer. This assumption allows the particles to be treated as inert tracers whose dynamics are governed primarily by drag, gravity, and inertia. To characterize particle–gas coupling, the Stokes number $\mathrm{St} = \tau_{\mathrm{p}} U/L$ was employed. For $\mathrm{St} < 1$, particles closely follow the gas streamlines, whereas higher values indicate increasing inertial deviation and enhanced probability of wall interception.

It should be emphasized that the present DPM framework aims to provide qualitative insights into particle transport and interception trends, rather than quantitative prediction of chemical interactions or deposition efficiencies.

3.5 Numerical implementation and validation

All governing equations were solved using the pressure-based solver with the finite volume method. Pressure – velocity coupling was handled using the PISO algorithm.[40] Second-order upwind schemes were applied for momentum, energy, volume fraction, and species transport, while the PRESTO! scheme was adopted for pressure discretization. Convergence was achieved when all residuals dropped below 10^{-5} and the wall heat flux reached steady values.

Grid independence was assessed by systematically refining meshes near the cooled wall. As shown in Fig. 4, when the total cell number exceeded 40 000, the predicted surface-averaged condensation heat–transfer coefficient exhibited negligible variation. Considering both computational efficiency and numerical accuracy, a mesh containing 46 800 cells was selected for all simulations.

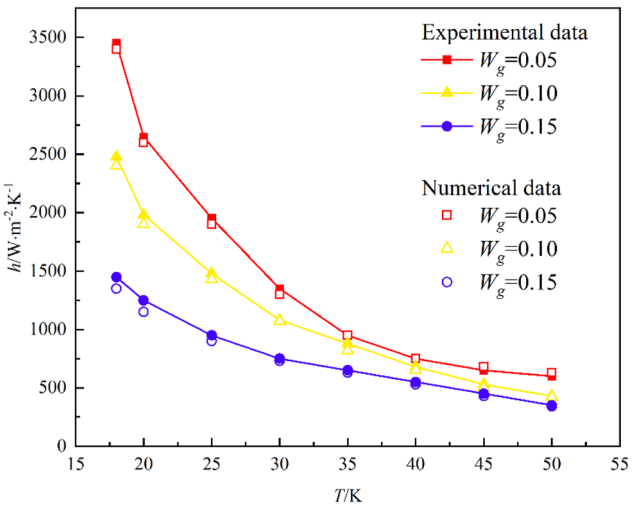

Fig. 5 Comparison between simulation and experimental data.

4. Results and discussion

Based on the proposed condensation model, the following results elucidate the coupled evolution of vapor–liquid interface dynamics, heat–mass transfer characteristics, and impurity transport behavior within undiluted $VOCl_3$-N_2-solid multiphase flows.

4.1 Model verification

4.1.1 Validation against experimental data. Due to the lack of experimental data for condensation of undiluted $VOCl_3$ vapor, the present model was validated using well-documented water–air condensation cases under comparable thermal and hydrodynamic conditions. Numerical predictions were compared with the experimental measurements of Yi *et al.*[41] and the analytical solutions reported by Minkowycz.[13]

As shown in Fig. 5, the predicted wall condensation heat-transfer coefficients at subcoolings of 20–50 K and air mass fractions of 5–15% exhibit excellent agreement with experimental data, with deviations below 7%. This consistency confirms that the implemented phase-change model accurately captures the dominant transport mechanisms governing vapor-NCG condensation, thereby providing a reliable foundation for extending the framework to $VOCl_3$ systems.

Although the validation case involves a water–air system, the governing mechanisms of condensation—interfacial mass transfer, latent heat release, and diffusion-driven vapor transport—are physically equivalent to those occurring in the $VOCl_3$–N_2 system under the studied operating conditions.

$$h = \frac{q''}{T_{sat} - T_w} \tag{16}$$

4.1.2 Validation against 3D model. To evaluate the rationality of the two-dimensional (2D) approximation, a three-dimensional (3D) model with identical geometric dimensions and boundary conditions is established for comparison, as illustrated in Fig. 6(a). The condensation of $VOCl_3$/nitrogen mixture is simulated under representative operating conditions.

Fig. 6(b) and (c) compare the distributions of the local heat–transfer coefficient and liquid-film thickness predicted by the 2D and 3D models along the flow direction. The results show excellent agreement, with negligible discrepancies over the entire condensation length. Furthermore, the transverse distribution of nitrogen mass fraction remains nearly uniform, as shown in Fig. 6(d), indicating weak spanwise transport.

These results demonstrate that the dominant transport processes mainly evolve in the streamwise direction. Therefore, the simplified 2D model is sufficient to capture the essential features of flow, heat transfer, and phase change, while significantly reducing computational cost.

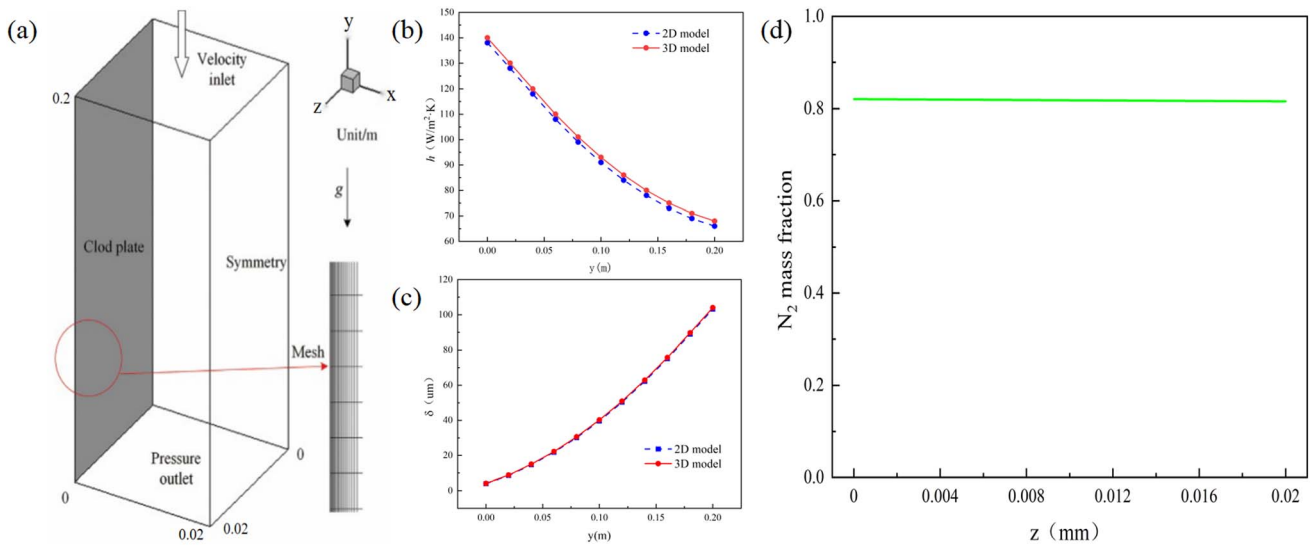

Fig. 6 Three-dimensional model and validation of the two-dimensional approximation: (a) computational domain and mesh; (b) local heat – transfer coefficient; (c) liquid-film thickness; (d) transverse distribution of N_2 mass fraction.

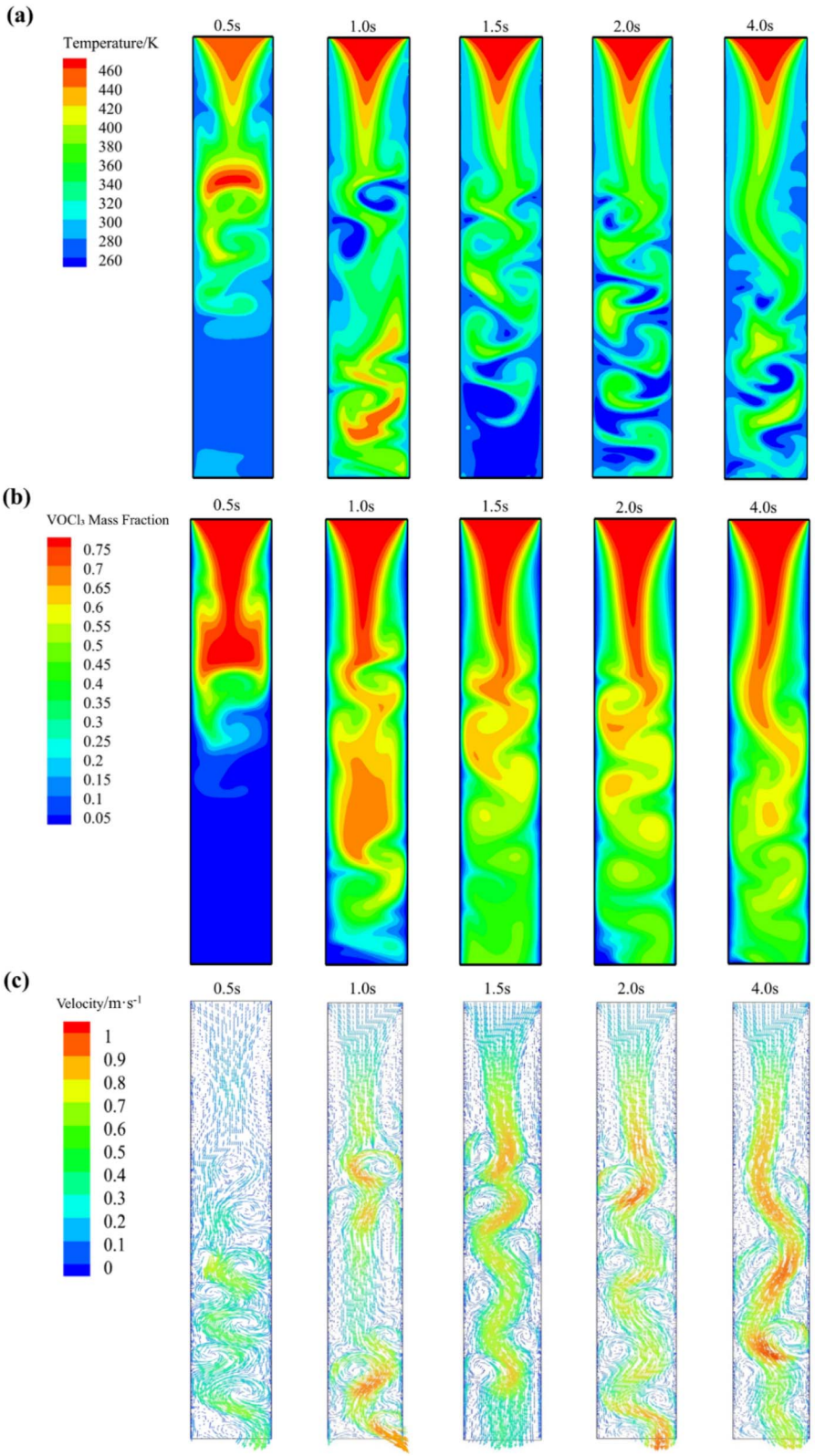

Fig. 7 Transient distribution of multiphysics fields during the distill-condensation process of $VOCl_3$ undiluted fluid: (a) temperature contours; (b) $VOCl_3$ vapor mass fraction contours; (c) velocity contours.

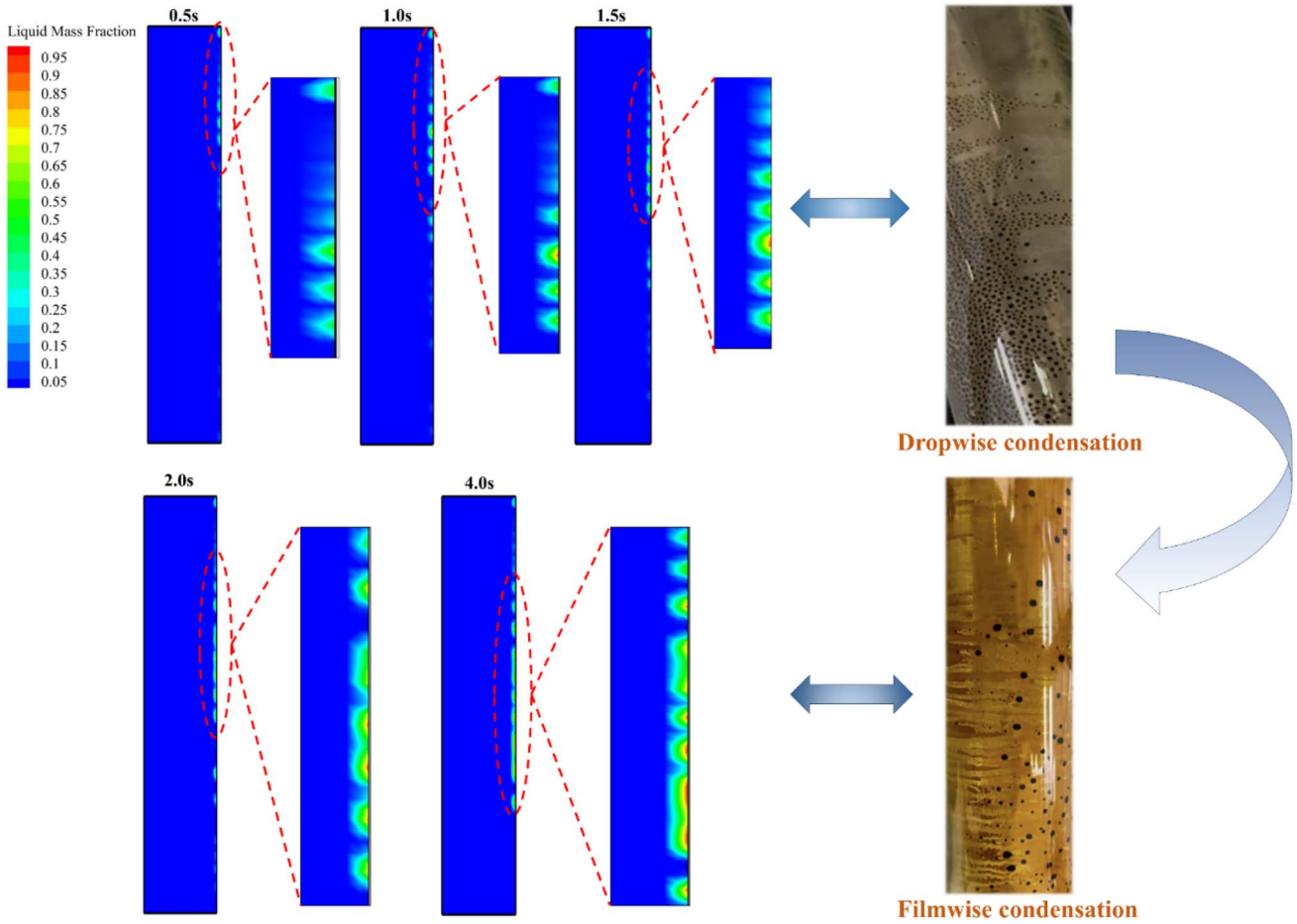

Fig. 8 Local distribution of liquid volume fraction and comparison with experimental condensate morphology.

4.2 Flow field structure and overall distill-condensation behavior

Fig. 7 illustrates the transient evolution of temperature, vapor concentration, and velocity fields. At the initial stage ($t = 0.5$ s), steep temperature gradients develop near the cooled wall, inducing localized condensation and generating strong thermal non-uniformity. As condensation proceeds ($t = 1$–2 s), a distinct thermal stratification emerges, characterized by a cold near-wall condensation zone and a high-temperature vapor core.

Correspondingly, the $VOCl_3$ mass fraction decreases sharply adjacent to the wall, forming a pronounced diffusion boundary layer that thickens over time. This behavior reflects the accumulation of nitrogen near the interface, which progressively enhances mass-transfer resistance. The flow field exhibits transient vortical structures during early stages, promoting interfacial mixing, while gradually transitioning to a smoother quasi-laminar pattern as the liquid film develops.

These results demonstrate the highly localized and spatially non-uniform characteristics of $VOCl_3$ condensation, governed by the coupled evolution of temperature, concentration, and hydrodynamic fields.

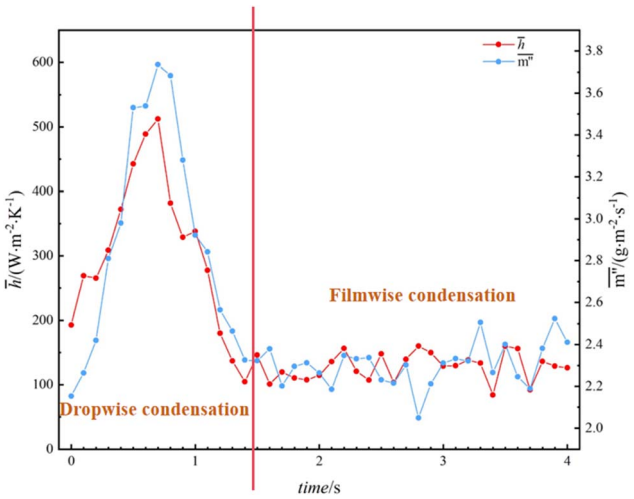

Fig. 9 Temporal variations of average condensation heat transfer coefficient and mass flux.

4.3 Evolution of interfacial structure and condensation intensity

The spatial distribution of liquid volume fraction (Fig. 8) reveals a clear evolution of interfacial structures along the cooled wall. At the initial stage, condensation is highly localized, with discrete liquid regions forming near the wall. As condensate accumulation increases, these liquid regions expand and

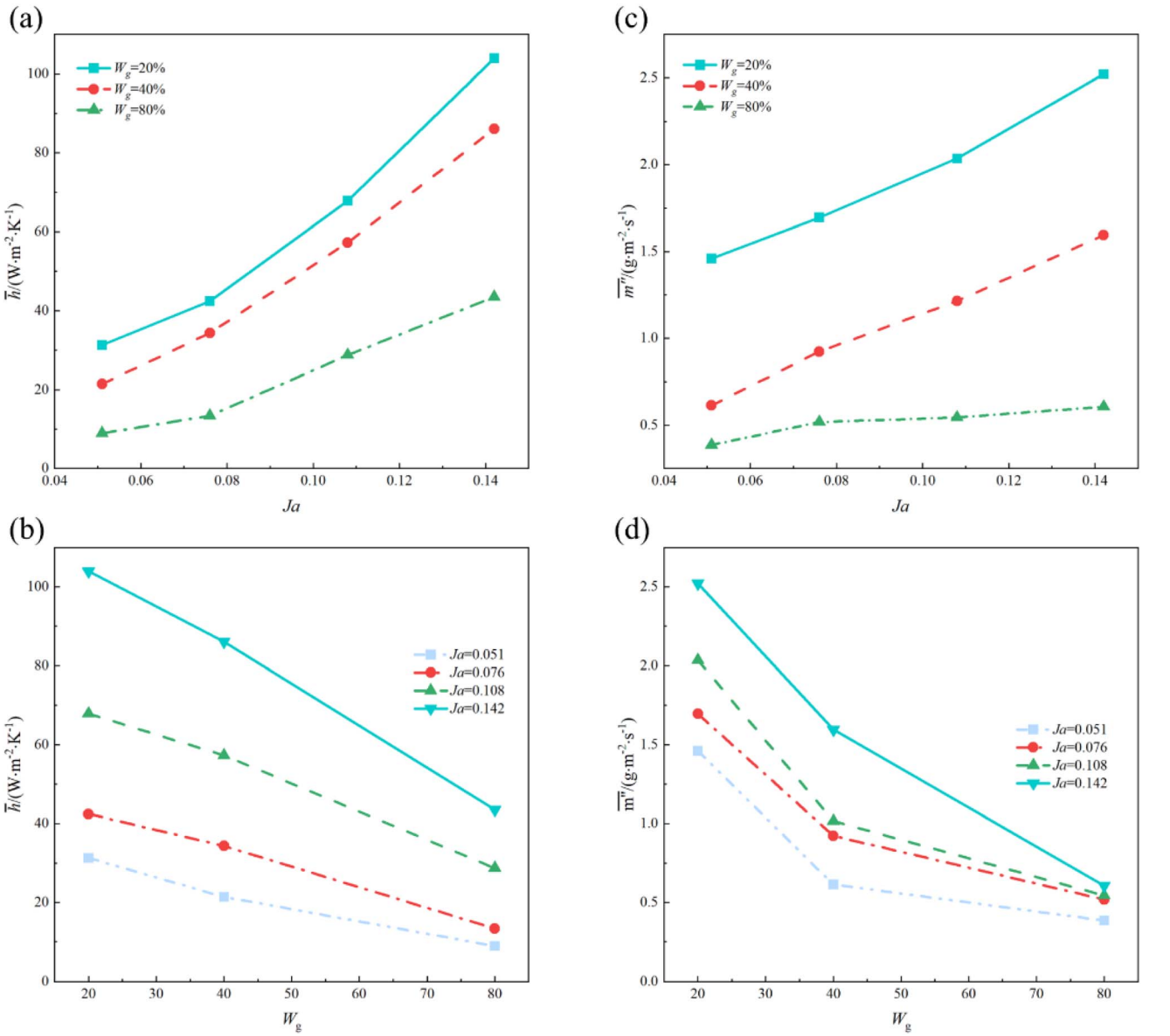

Fig. 10 Effect of NCG concentration and Jakob number on condensation performance: (a) $\bar{h}$ *vs.* Ja at different NCG concentrations; (b) $\bar{h}$ *vs.* NCG concentration at different Ja; (c) $\overline{\dot{m}''}$ *vs.* Ja at different NCG concentrations; (d) $\overline{\dot{m}''}$ *vs.* NCG concentration at different Ja.

merge, gradually developing into a continuous liquid film downstream.

This interfacial evolution reflects the self-regulating nature of the condensation process: latent heat release weakens local wall subcooling, while nitrogen enrichment thickens the diffusion boundary layer, collectively smoothing interfacial gradients and reducing condensation intensity. As a result, the condensation regime progressively transitions from a localized, interface-controlled mode toward a diffusion-limited film-dominated state.

The temporal evolution of surface-averaged heat–transfer coefficient $\bar{h}$ and condensation mass flux $\overline{\dot{m}''}$ is shown in Fig. 9. Initially, strong condensation occurs due to high thermal driving potential and minimal diffusion resistance. As the liquid film thickens, thermal resistance increases, leading to a gradual decline in both $\bar{h}$ and $\overline{\dot{m}''}$. Under steady conditions, $\bar{h}$ ranges from approximately 50 to 130 W m^{-2} K^{-1}, increasing markedly with decreasing wall temperature.

$$\bar{h} = \frac{1}{A_i}\int_{A_i} h_c \mathrm{d}A = \frac{1}{(T_{sat} - T_w)} \cdot \frac{\sum q_i'' A_i}{\sum A_i} \tag{17}$$

$$\overline{\dot{m}''} = \frac{1}{A_i}\int_{A_i} \dot{m}'' \mathrm{d}A = \frac{\sum \rho_l v_n A_i}{\sum A_i} \tag{18}$$

4.4 Effect of NCG concentration and wall subcooling

Fig. 10 presents the variations of surface-averaged $\bar{h}$ and $\overline{\dot{m}''}$ under different nitrogen concentrations and wall subcoolings,

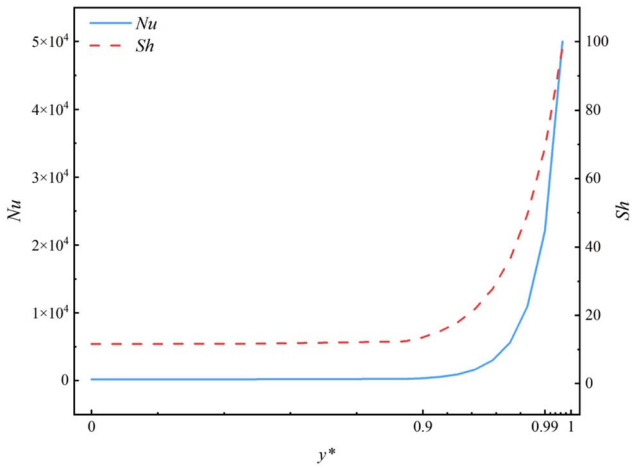

Fig. 11 Local Nusselt and Sherwood number distributions along the flow path.

characterized by the Jakob number Ja. Increasing NCG fraction significantly suppresses condensation, as nitrogen accumulation near the interface enhances diffusion resistance. Conversely, larger wall subcooling intensifies condensation by increasing the thermal driving force.

Quantitatively, when Ja = 0.142, increasing the NCG mole fraction from 20% to 80% reduces $\bar{h}$ by approximately 43%. At fixed NCG content, increasing Ja from 0.051 to 0.142 enhances condensation intensity by about 35%. This competitive coupling between diffusion resistance and thermal potential governs the spatial non-uniformity of condensation and underlies the observed transition of interfacial structure and condensation regime.

To further characterize local transport behavior, dimensionless Nusselt and Sherwood numbers were evaluated (Fig. 11). Both quantities decrease monotonically along the flow direction, indicating progressive weakening of heat and mass transfer as the diffusion boundary layer thickens. The similarity of their spatial trends highlights the strong coupling between thermal and concentration fields during $VOCl_3$ condensation.

4.5 Solid particle behavior and impurity migration

During $VOCl_3$ condensation under nitrogen protection, fine solid impurities are entrained in the vapor stream and transported into the condensation region. Fig. 12 shows the predicted particle trajectories and residence-time distributions for these particles.

Overall, all particle types exhibit dominant downward transport following the carrier-gas flow, with residence times mainly concentrated within 0–4 s. Local recirculation structures induce minor clustering in low-velocity regions, but no significant deposition or adhesion is observed. NaCl particles, possessing the smallest size and lowest density, display the strongest flow-following behavior and maintain relatively uniform distributions. Heavier particles such as $FeCl_3$ and $MgCl_2$ exhibit slightly increased near-wall residence due to inertial effects, while their outlet recovery rates remain above 99%, indicating limited overall deposition.

$AlCl_3$ particles show a slightly lower outlet recovery rate (98.7%) compared with the other particle types. Although the difference is relatively small, it may indicate a weak tendency for increased near-wall residence associated with particle inertia and local interfacial flow structures.

Table 2 summarizes the statistical characteristics of particle motion. Average particle velocities range from 0.91 to 0.98 $m \cdot s^{-1}$, and residence times vary between 1.06 and 1.18 s. These numerical trends agree well with the ICP measurements of trace impurities in the condensed $VOCl_3$ product, which reveal low residual contents of Fe (0.006%), Mg (0.005%), Na (0.010%), and Al (0.045%). The slightly elevated Al concentration may reflect a weak tendency for interaction between Al-containing particles and the developing condensate film, although the difference remains relatively small.

Overall, the entrained solids exert limited influence on the global condensation performance under the present operating conditions, while their transport and redistribution by the evolving flow and interfacial structures may induce localized impurity enrichment in the condensate. These findings provide mechanistic insight into impurity migration and offer quantitative guidance for optimizing industrial purification strategies.

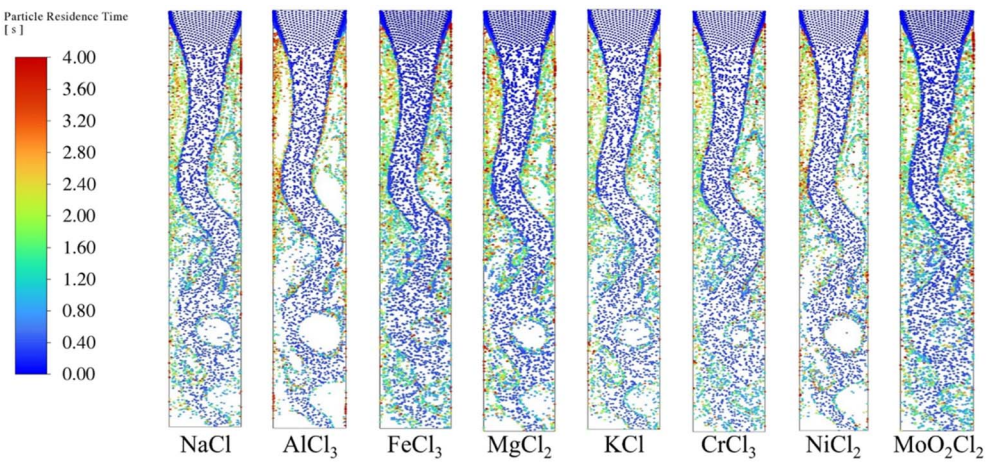

Fig. 12 Particle trajectories and residence time distributions.

Table 2 Statistical results of particle motion characteristics under typical condition

Particle type	Average velocity/m s^{-1}	Average residence time/s	Outlet recovery rate/%
NaCl	0.96	1.06	99.24
$AlCl_3$	0.98	1.18	98.70
$FeCl_3$	0.94	1.10	99.65
$MgCl_2$	0.92	1.12	99.70
KCl	0.97	1.05	99.75
$NiCl_2$	0.95	1.09	99.80
$CrCl_3$	0.93	1.11	99.85
MoO_2Cl_2	0.91	1.14	99.88

5. Conclusions

A coupled VOF-Species Transport-Discrete Phase numerical framework incorporating user-defined condensation source terms (UDFs) was developed to systematically investigate the multiphase condensation and impurity migration behaviors of $VOCl_3$ mixed vapors under nitrogen-protected conditions. The main conclusions can be summarized as follows:

1 $VOCl_3$ vapor exhibits an initially localized and discontinuous condensation pattern near the cooled wall, which gradually evolves into a continuous liquid film along the flow direction. This morphological transition significantly reduces interfacial renewal and heat-transfer intensity, revealing an inherent evolution from localized condensation toward a diffusion-controlled regime.

2 Nitrogen accumulation in the vicinity of the condensation interface substantially thickens the diffusion boundary layer and increases mass-transfer resistance, resulting in pronounced deterioration of both local and surface-averaged heat-transfer coefficients. In contrast, enhanced wall subcooling strengthens the thermal driving force and effectively promotes condensation. The competition between these two effects governs the spatial non-uniformity and intermittent nature of the condensation process.

3 The synchronized decay of local Nusselt and Sherwood numbers along the flow direction confirms the parallel attenuation of heat and mass transfer capabilities. This correspondence indicates that the overall condensation performance is governed by a unified thermodynamic – diffusive coupling mechanism.

4 Most entrained solid impurity particles are transported predominantly along the gas-phase streamlines, yielding outlet recovery rates exceeding 99%, which demonstrates that their presence exerts only a negligible influence (<5%) on the global condensation dynamics. Among the investigated species, $AlCl_3$ exhibits a weak yet noticeable tendency to accumulate near the cooled wall, primarily attributed to its moderate particle inertia and its enhanced sensitivity to near-wall flow and concentration gradients under strong thermal and concentration gradients near the condensation interface. This behavior is consistent with ICP measurements showing a slightly elevated aluminum fraction in the condensate, suggesting that the developing liquid film may function as a passive physical interception layer capable of partially capturing solid impurity particles during the distillation–condensation process.

5 For industrial-scale condensers, several additional factors should be considered, including larger Reynolds numbers, stronger hydrodynamic instabilities, and potential three-dimensional flow structures. These effects may modify the thickness of the diffusion boundary layer and alter local condensation intensity. Nevertheless, the fundamental diffusion-controlled mechanism identified in this study is expected to remain valid, providing useful guidance for scale-up design and optimization.

Author contributions

Zeli Yang: conceptualization, investigation, methodology, writing – original draft, writing – review & editing. Yong Fan: writing – review & editing, supervision. Yimin Zhang: writing – review & editing, supervision. Qiushi Zheng: writing – review & editing, supervision. Peng Liu: investigation. Jiang Huang: investigation.

Conflicts of interest

The authors declare that they have no known competing financial interests or personal relationships that could have appeared to influence the work reported in this paper.

Data availability

The data supporting the findings of this study are available from the corresponding author upon reasonable request.

Acknowledgements

This work was financially supported by the Project of National Natural Science Foundation of China (52374274), the National Key R&D Program of China (2021YFC2901600), and the Hubei Province Science and Technology Program (2024EHA009). Special Thanks to the Germany Alexander von Humboldt Stiftung and the Japan Society for the Promotion of Science.

References

1 D. W. B. Westerman, I. E. Ruffio, M. S. Wainwright and N. R. Foster, Chemical analysis of vanadium pentoxide catalysts, *Anal. Chim. Acta*, 1980, **117**, 285–291.

2 M. Dassisti, P. Mastrorilli, A. Rizzuti, G. Cozzolino, M. Chimienti, A.-G. Olabi, F. Matera, A. Carbone and M. Ramadan, Vanadium: A transition metal for sustainable energy storing in redox flow batteries, in *Encyclopedia of Smart Materials*, ed. A.-G. Olabi, Elsevier, Oxford, 2022, pp. 208–229.

3 Y. Lv, C. Han, Ye Zhu, T. Zhang, S. Yao, Z. xing He, L. Dai and L. Wang, Recent advances in metals and metal oxides as catalysts for vanadium redox flow battery: Properties, structures, and perspectives, *J. Mater. Sci. Technol.*, 2021, **75**, 96–109.

4 T. Khac Le, M. Kang and S. W. Kim, A review on the optical characterization of V2O5 micro-nanostructures, *Ceram. Int.*, 2019, **45**(13), 15781–15798.

5 H. Gamal, A. M. Elshahawy, S. S. Medany, M. A. Hef-nawy and M. S. Shalaby, Recent advances of vanadium oxides and their derivatives in supercapacitor applications: A comprehensive review, *J. Energy Storage*, 2024, **76**, 109788.

6 Y. Zhang, W. Bo, Q. Zheng, T. Liu, N. Xue, P. Hu and H. Liu, A review of processing and utilization technology for vanadium shale resources, *Sep. Purif. Technol.*, 2025, **379**, 135185.

7 T. Klahm, Heat transfer during reflux condensation of an R134a/R123 mixture, *Int. J. Refrig.*, 2010, **33**(3), 498–506.

8 K. Hogan, V. M. Patel and P. F. Peterson, Implementation of a generalized diffusion layer model for condensation of vapor with non-condensable gases, *Int. J. Heat Mass Transfer*, 2010, **53**(21–22), 4843–4855.

9 W. Liu, H. Zhang, Y. Li and X. Chen, Heat-transfer model based on diffusion-layer theory for dropwise condensation with non-condensable gas, *AIP Adv.*, 2020, **10**, 125305.

10 D. W. Shao and E. Granryd, Experimental and theoretical study on flow condensation with non-azeotropic refrigerant mixtures of R32/R134a, *Int. J. Refrig.*, 1998, **21**(3), 230–246.

11 D. Jin, J. Kwon and M. Kim, Prediction of in-tube condensation heat transfer characteristics of binary refrigerant mixtures, *Int. J. Refrig.*, 2003, **26**(6), 593–600.

12 W. Nusselt, The surface condensation of water vapour, *Z. Des. Vereines Dtsch. Ingenieure*, 1916, **60**, 541–546.

13 W. J. Minkowycz and E. M. Sparrow, Condensation heat transfer in the presence of non-condensables, interfacial resistance, superheating, variable properties, and diffusion, *Int. J. Heat Mass Tran.*, 1966, **9**(10), 1125–1144.

14 A. P. Colburn and O. A. Hougen, Design of cooler condensers for mixtures of vapors with noncondensing gases, *Ind. Eng. Chem.*, 1934, **26**(11), 1178–1182.

15 A. P. Colburn and O. A. Hougen, Studies in Heat Transmissionll-Measurement of Fluid and Surface Temperatures, *Ind. Eng. Chem.*, 1930, **22**(5), 522–524.

16 A. P. Colburn and O. A. Hougen, Design of Cooler Condensers for Mixtures of Vapors with Noncondensing Gases, *Ind. Eng. Chem.*, 1934, **26**(11), 1178–1182.

17 V. E. Denny, A. F. Mills and V. J. Jusionis, Laminar Film Condensation From a Steam-Air Mixture Undergoing Forced Flow Down a Vertical Surface, *J. Heat Transfer*, 1971, **93**(3), 297.

18 V. E. Denny and V. J. Jusionis, Effects of non-condensable gas and forced flow on laminar film condensation, *Int. J. Heat Mass Tran.*, 1972, **15**(2), 315–326.

19 S. Oh and S. T. Revankar, Experimental and theoretical investigation of film condensation with non-condensable gas, *Int. J. Heat Mass Tran.*, 2006, **49**(15), 2523–2534.

20 S. Kuhn. *Investigation of Heat Transfer from Condensing Steam-Gas Mixture and Turbulent Films Flowing Downward inside a Vertical tubes[D]. Ph. D. Dissertation*, University of California at Berkeley, 1995.

21 S. Z. Kuhn, V. E. Schrock and P. F. Peterson, An investigation of condensation from steam gas mixtures flowing downward inside a vertical tube, *Nucl. Eng. Des.*, 1997, **177**(1), 53–69.

22 V. E. Denny and A. F. Mills, Non-similar solutions for laminar film condensation on a vertical surface, *Int. J. Heat Mass Tran.*, 1969, **12**(8), 965–979.

23 K. Lucas, Combined body force and forced convection in laminar film condensation of mixed vapours-integral and finite difference treatment, *Int. J. Heat Mass Transfer*, 1976, **19**(11), 1273–1280.

24 D. X. Jin, J. T. K won and M. H. Kim, Prediction of in-tube condensation heat transfer characteristics of binary refrigerant mixtures, *Int. J. Refrig.*, 2003, **26**(5), 593–600.

25 Z. Zhang, Q. Li, T. Xu, X. Fang and X. Gao, Condensation heat transfer characteristics of zeotropic refrigerant mixture R407C on finned/helical tubes, *Appl. Therm. Eng.*, 2012, **39**, 63–72.

26 B. Thonon and A. Bontemps, Condensation of pure and mixture of hydrocarbons in a compact welded plate heat exchanger—experiments and modelling, *Int. J. Refrig.*, 2002, **25**(3), 305–314.

27 J. Yu, X. Ma, Y. Chen and Q. Wang, Numerical investigation on flow condensation of methane/propane and ethane/propane mixtures in helical tubes, *Appl. Therm. Eng.*, 2018, **134**, 73–85.

28 J. Yu, Y. Jiang, W. Cai and X. Ma, Numerical investigation on flow condensation of zeotropic hydrocarbon mixtures in a helically coiled tube, *Appl. Therm. Eng.*, 2018, **134**, 322–332.

29 S. Li, W. Cai, J. Chen and H. Zhang, Numerical study on condensation heat transfer and pressure drop characteristics of ethane/propane mixture upward flow in a spiral pipe, *Int. J. Heat Mass Transfer*, 2018, **121**, 170–186.

30 S. Li, W. Cai, J. Chen, H. Zhang and Y. Jiang, Numerical study on the flow and heat transfer characteristics of forced convective condensation with propane in a spiral pipe., *Int. J. Heat Mass Transfer*, 2018, **117**, 1169–1187.

31 X. R. Zhuang, G. F. Chen, H. Guo, Q. L. Song, Q. X. Tang, Z. Q. Yang, X. Zou and M. Q. Gong, Experimental investigation on flow condensation of zeotropic mixtures of methane/ethane in a horizontal smooth tube, *Int. J. Refrig.*, 2018, **85**, 120–134.

32 S. L. Zhu, Y. Li, R. P. Zhang, Y. Tang, L. M. Qiu and X. Q. Zhi, Experimental study on the con-densation characteristics of nitrogen with non-condensable gas, *Cryogenics*, 2019, **98**, 29–38.

33 S. Zhu, Y. Tang, C. Gu, Y. Li, X. Zhi and L. M. Qiu, Visualization experiment and numerical simulation of

nitrogen-neon mixture condensation, *Appl. Therm. Eng.*, 2020, **164**, 114492.
34 C. W. Hirt and B. D. Nichols, Volume of Fluid (VOF) Method for the Dynamics of Free Boundaries, *J. Comput. Phys.*, 1981, **39**, 201–225.
35 S. Chapman and T. G. Cowling, *The Mathematical Theory of Non-uniform Gases*, Cambridge University Press, Cambridge, 3rd edn, 1970.
36 K. Hogan, *et al.*, Implementation of a generalized diffusion layer model for condensation of vapor with non-condensable gases, *Int. J. Heat Mass Transfer*, 2010, **53**, 4843–4855.
37 S. M. Kim and I. Mudawar, Review of databases and predictive methods for heat transfer in condensing and boiling flows, *Int. J. Heat Mass Transfer*, 2014, **77**, 627–652.
38 E. W. Lemmon, M. L. Huber and M. O. McLinden, *REFPROP: Reference Fluid Thermodynamic and Transport Properties Database, Version 9.1, Standard Reference Database*, National Institute of Standards and Technology (NIST), Gaithersburg, MD, USA, vol. 23, 2013.
39 R. Clift, J. R. Grace and M. E. Weber, Drag Coefficient and Motion of Spherical Particles, *J. Fluid Mech.*, 1972, **55**, 193–208.
40 R. I. Issa, Solution of the Implicitly Discretised Fluid Flow Equations by Operator-Splitting, *J. Comput. Phys.*, 1986, **62**, 40–65.
41 Q. Yi, M. Tian, W. Yan, X. Qu and X. Chen, Visualization study of the influence of non-condensable gas on steam condensation heat transfer, *Appl. Therm. Eng.*, 2016, **106**, 13–21.